
Fix False Transparency by Noise Guided Splatting

Aly El Hakie^{1*}, Yiren Lu^{2*}, Yu Yin², Michael Jenkins^{1,2}, Yehe Liu^{1,2}

¹OpsiClear LLC

²Case Western Reserve University

¹{aly, yehe}@opsiclear.com

²{yiren.lu, yu.yin, mwj5}@case.edu

<https://opsiclear.github.io/ngs/>

Abstract

Opaque objects reconstructed by 3D Gaussian Splatting (3DGS) often exhibit a falsely transparent surface, leading to inconsistent background and internal patterns under camera motion in interactive viewing. This issue stems from the ill-posed optimization in 3DGS. During training, background and foreground Gaussians are blended via α -compositing and optimized solely against the input RGB images using a photometric loss. As this process lacks an explicit constraint on surface opacity, the optimization may incorrectly assign transparency to opaque regions, resulting in view-inconsistent and falsely transparent. This issue is difficult to detect in standard evaluation settings (*i.e.*, rendering static images) but becomes particularly evident in object-centric reconstructions under interactive viewing. Although other causes of view-inconsistency (*e.g.*, popping artifacts) have been explored recently, false transparency has not been explicitly identified. To the best of our knowledge, we are the first to identify, characterize, and develop solutions for this "false transparency" artifact, an underreported artifact in 3DGS. Our strategy, Noise Guided Splatting (NGS), encourages surface Gaussians to adopt higher opacity by injecting opaque noise Gaussians in the object volume during training, requiring only minimal modifications to the existing splatting process. To quantitatively evaluate false transparency in static renderings, we propose a transmittance-based metric that measures the severity of this artifact. In addition, we introduce a customized, high-quality object-centric scan dataset exhibiting pronounced transparency issues, and we augment popular existing datasets (*e.g.*, DTU) with complementary infill noise specifically designed to assess the robustness of 3D reconstruction methods to false transparency. Experiments across multiple datasets show that NGS substantially reduces false transparency while maintaining competitive performance on standard rendering metrics (*e.g.*, PSNR), demonstrating its overall effectiveness.

1 Introduction

3D Gaussian Splatting (3DGS) [1] is an emerging neural rendering technique offering unprecedented real-time performance and fidelity through explicit scene representation. However, due to its unconstrained optimization and the α -blending process, opaque surface Gaussians can be incorrectly learned as transparent, a phenomenon we refer to as false transparency.

False transparency causes opaque surfaces to incorrectly appear semi-transparent, especially observable during interactive viewing and undetectable in individual frames and standard Image Quality Assessment (IQA) metrics. The phenomenon manifests as a parallax-induced transparency effect:

* These authors contribute equally.

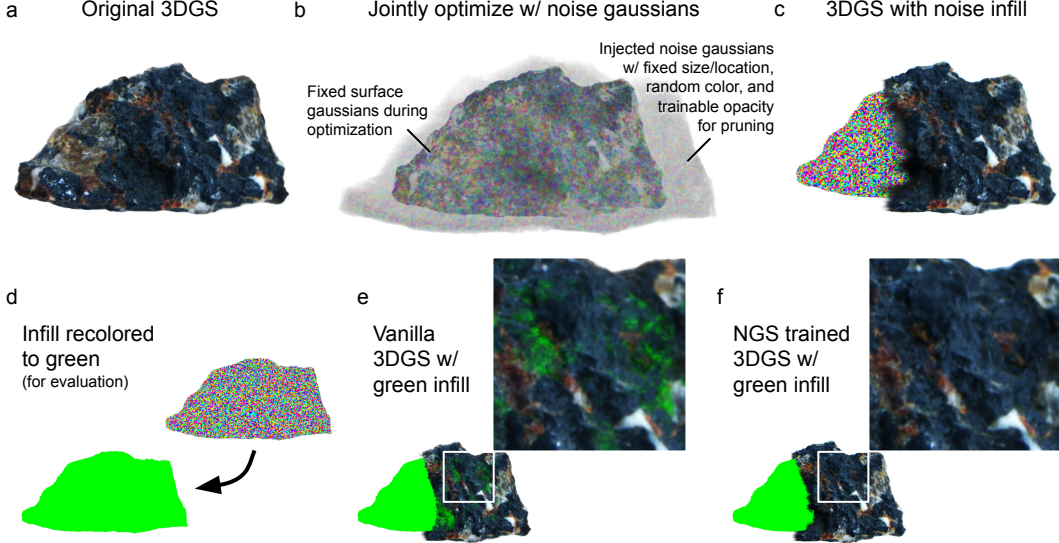


Figure 1: Overview of the NGS. (a) Object-centric 3DGS render of a stone. (b) Noise Gaussians are introduced to the training process. (c) Only visible noise are removed during optimization, leaving subsurface noise filling the object. (d) Noise infill can be recolored and saved for transparency evaluation. (e) Recolored infill inserted to the vanilla 3DGS revealing highly transparent regions on the surface. (f) Recolored infill does not leak through the NGS trained surface.

during camera movement, objects exhibit a disturbing "see-through" quality where internal and background Gaussian structures become visible through surfaces that should be opaque. These internal structures move out of alignment with the surface under changes in camera pose, creating an illusion reminiscent of frosted glass.

This false transparency artifact occurs because 3DGS is supervised primarily by a 2D photometric loss between rendered and ground-truth images. Such supervision creates ambiguity regarding true surface opacity, as the optimization can jointly refine foreground and inner background elements in discrete views, with their combined rendering still satisfying the 2D constraints.

This false transparency is most commonly observed in regions lacking adequate visual cues to differentiate between an opaque surface and a semi-transparent surface backed by another surface, specifically in areas presenting low texture, repeating patterns, specular highlights, or geometric complexity. The problem is also more pronounced in object-centric reconstruction. In scene-level reconstruction, many objects are not imaged from all angles and lack information about their posterior surfaces, resulting in less ambiguity. However, in 360° object-centric settings, the mean depth between opposing surfaces is small. Every front-facing surface is paired with a back surface along the same ray, causing both to be optimized jointly. Besides visual artifacts, false transparency also affects downstream applications such as surface extraction, physics simulations, and volumetric analysis. Because these applications rely on accurate opacity to delineate object boundaries, an ambiguous alpha causes invalid or unreliable results.

The problem of false transparency in 3DGS is largely unacknowledged and not fully understood. In practice, evaluating the severity of this false transparency is challenging during both training and post-training analysis, as conventional metrics generally rely on comparing static renderings with 2D reference. Some recent studies [2, 3, 4, 5, 6] have indirectly mitigated this issue. Although these studies advanced approximation techniques in the splatting process, for example by refining depth-ordering and α -blending, their main goal was to improve view-consistency in 3DGS. As such, they did not directly address the underlying mechanisms responsible for false transparency.

This paper introduces Noise Guided Splatting (NGS) (Fig. 1), a novel strategy to address the opacity ambiguity during optimization. Our method establishes persistent internal noise Gaussian structures within an object's volume, effectively enforcing surface opacity. NGS allocates high-opacity noise Gaussians with continuously randomized coloration within the object's volume. The infill creates

an effective occlusion barrier between opposing surfaces, preventing the optimization process from integrating back surfaces into the front-facing rendering. Additionally, the noise point cloud can be extracted, recolored, and repurposed as a diagnostic tool to support evaluating false transparency when assessing any splatting-based rendering methods. In summary, we make the following contributions:

1. A new technique that places interior noise Gaussians to distinguish between the interior and exterior space of the rendered object, guiding optimization toward proper surface opacity. The method is plug-and-play and requires minimal modifications to existing frameworks.
2. A new approach to visualize and quantify the false transparency in static 3DGS renderings.
3. A noise Gaussian infill dataset, including infill add-ons to existing datasets (e.g., DTU) and a customized high-resolution object-centric scan dataset, to facilitate benchmarking.

2 Related works

Novel View Synthesis (NVS). Neural Radiance Fields (NeRF) [7] revolutionized NVS through neural implicit representations for 3D scenes, achieving high visual quality. However, NeRF’s computational demands led to the development of faster alternatives like sparse voxel grids [8] and hash encoding [9]. 3DGS [1] marked a major advancement through explicit trainable primitives, enabling real-time rendering with high fidelity. Building upon 3DGS, numerous works have enhanced its capabilities in numerous directions, including more efficient training strategies [10, 11], better densification heuristics [12], anti-aliasing [13] and reduced dependency on initialization [14].

NVS artifacts. There are several well recognized NVS artifacts that should not be confused with false transparency artifacts. A common one is floater artifacts, which manifest as sparse features reconstructed at incorrect depths above the surface [15, 16]. These artifacts do not appear in training views but become obvious in novel views. Floaters have been successfully mitigated using depth consistency constraints [15, 17] and specialized priors [16, 18, 19]. Another category is view-inconsistency artifacts, which cause surfaces to exhibit unnatural changes during viewpoint transitions. A well-known example is the ‘popping artifact’ [6], caused by sorting discontinuities between adjacent views. Hierarchical sorting [6], order-independent transparency [2], anti-aliasing filtering [4], and hybrid transparency [5] have been introduced to address these problems. Finally, 3DGS also suffers from poor reconstruction of certain details, which has been addressed using specialized loss functions [20] and diffusion-based post-processing enhancements [21].

Transparency. Blending semi-transparent primitives is an essential feature of 3DGS, ensuring rendering fidelity and smooth transitions across viewing angles. Most research on 3DGS transparency focuses on accurately reconstructing inherently transparent objects [22, 23, 24]. However, the phenomenon of false transparency, where surfaces intended to be opaque incorrectly appear transparent, remains largely unexplored in the literature. This oversight is significant because false transparency contributes substantially to view inconsistency artifacts through a different mechanism from popping.

Object-centric reconstruction. Scene reconstructions mostly reconstruct the front side of some objects. In contrast, object-centric techniques scan around the target object, and often have the object isolated from the scene. Some methods use object masks for targeted reconstruction [25, 26, 27], while others employ semantic segmentation or prompt-based interaction [28, 29, 30, 31]. These advancements have enabled object-aware representations, manipulation [32, 33], and improved 3D asset editing [34, 35]. However, accurately defining object boundaries in complex scenes with occlusions, transparencies, and intricate geometries remains challenging.

3 Theories & Methods

3.1 False-transparency mechanism

Background. In the original 3DGS pipeline [1], each pixel value is obtained by front-to-back α -blending of the depth-sorted splats whose projection cover that pixel:

$$C(p) = \sum_{i \in \mathcal{N}(p)} \alpha_i c_i \prod_{j < i} (1 - \alpha_j), \quad (1)$$

where $\alpha_i \in [0, 1]$ and $c_i \in \mathbb{R}^3$ are the opacity and color of splat i and $\mathcal{N}(p)$ is the front-to-back list along the ray going through pixel p . Training minimizes a purely image-space objective with

compound L1 and SSIM loss:

$$\mathcal{L}_{\text{photo}} = (1 - \lambda) \frac{1}{|\mathcal{P}|} \sum_{\mathbf{p} \in \mathcal{P}} \|\mathbf{C}(\mathbf{p}; \Theta) - \mathbf{I}_{\text{GT}}(\mathbf{p})\|_1 + \lambda \mathcal{L}_{\text{D-SSIM}}, \quad (2)$$

with respect to all Gaussian parameters Θ . The photometric loss (Eq. (2)) constrains only the final RGB value and its local structure. It is indifferent to how the color is distributed along the ray.

Where the transparency ambiguity arises. Let s be the index of the first intersected surface splat and denote all deeper splats by \mathcal{B} . Decomposing (1) at s yields:

$$\mathbf{C}(\mathbf{p}) = \underbrace{\alpha_s \mathbf{c}_s}_{\text{front surface}} + \underbrace{(1 - \alpha_s) \sum_{i \in \mathcal{B}} \alpha_i \mathbf{c}_i \prod_{s < j < i} (1 - \alpha_j)}_{\text{background that leaks if } \alpha_s < 1}. \quad (3)$$

For every semi-transparent surface ($\alpha_s < 1$) there exists a set of background opacities/colors that reproduces the exact pixel color of a fully opaque surface, giving the same loss in Eq. (2). Gradient descent therefore can accept trivial minima with low α_s . In turn, the surface becomes translucent even though it should be opaque (Fig. 2).

3.2 Object-centric reconstruction

Alpha-consistency loss. Given a pre-computed binary mask we can suppress any opacity that spills outside the object. Let $\mathcal{P} = \{1, \dots, h w\}$ be the set of pixel indices, $A_i \in [0, 1]$ the rendered alpha and $M_i \in \{0, 1\}$ the mask. Following [25] we define the **background-suppression loss** $\mathcal{L}_b = \frac{1}{|\mathcal{P}|} \sum_{i \in \mathcal{P}} A_i (1 - M_i)$, which drives $A_i \rightarrow 0$ wherever the mask is zero.

Most 3DGS variants employ strategies that restrict opacity to reduce over-reconstruction. For instance, the original 3DGS resets opacity values [1], Markov Chain Monte Carlo (MCMC) densifies the point cloud using sampling from Gaussian opacity distribution [14], and Revised Adaptive Density Control (ADC) implements explicit opacity regularization [12]. All of these approaches unintentionally promote transparency in scenarios where internal background colors match object surface colors, because there is no photometric incentive to maintain surface consistency when the optimization can minimize loss by simply reducing opacity. Adapting the Revised ADC idea to the object mask yields the complementary **foreground-opacity loss** $\mathcal{L}_f = \frac{1}{|\mathcal{P}|} \sum_{i \in \mathcal{P}} (1 - A_i) M_i$, which rewards pixels inside the mask for reaching full opacity. Summing the two gives a single alpha-consistency loss \mathcal{L}_a , which is simply the L_1 distance because $A_i, M_i \in [0, 1]$:

$$\mathcal{L}_a = \mathcal{L}_f + \mathcal{L}_b = \frac{1}{|\mathcal{P}|} \sum_{i \in \mathcal{P}} |A_i - M_i|, \quad (4)$$

Limitations in 360° captures. For reconstructions from incomplete views of the object, \mathcal{L}_a cleanly separates object and background. In full 360° scans each camera ray almost always intersects with multiple surfaces. Gaussians behind the first surface are ‘background’ for that ray, but lie inside the mask for other views. Without an additional bias toward the front-most Gaussians, the optimizer sometimes have a tendency to converge to semi-transparent surfaces.

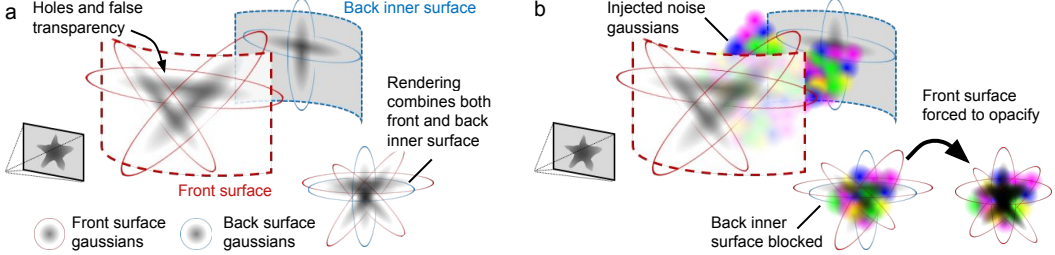


Figure 2: Mechanisms of false transparency and NGS. (a) A semi-transparent front surface and a inner back surface can jointly render to mimic a ground-truth images, causing the false transparency artifact. (b) NGS fills interior volume with colored noise Gaussians, promoting the surface opacity.

3.3 Noise Guided Splatting (NGS)

NGS addresses false transparency by employing an alpha consistency loss and strategically placing noise Gaussians within the object’s volume to obstruct direct lines of sight between front and back surfaces, as illustrated in Fig. 1, thereby forcing the optimization to prioritize an opaque foreground (Fig. 2) The pipeline begins by initializing a set of noise Gaussians within a coarse voxelized convex hull of the object. The color of the noise Gaussians are randomized in each iteration to prevent overfitting. These noise Gaussians are then pruned based on depth, ensuring only noise Gaussians inside the object remain. This initialization and pruning sequence is repeated in a multi-scale manner across increasing voxel resolutions to accurately fill complex geometries while remaining memory efficient. Afterwards, we conduct a brief fine tuning phase where the surface Gaussians are frozen, and the noise Gaussians opacities are trained and pruned. Finally, the noise Gaussians are frozen, the surface Gaussians are unfrozen and training proceeds normally with a reset learning rate.

Initialization. We first compute a convex hull mesh from the means of existing Gaussian primitives using Quickhull [36]. The mesh provides an approximation of the object’s volume that is then converted into a coarse occupancy volume. Voxels located inside the mesh are marked as occupied. We map each occupied voxel in this coarse voxel grid to a sparse noise point, and set it to a random color. The dense occupancy grid is always synced to the sparse point in downstream operations.

Pruning. The convex hull approximation includes regions outside the actual object. Therefore, for each rendered pixel in each view in the capture, we identify and remove noise Gaussians that appear in front of surface Gaussians using 3DGS’s depth ordering [1]. This carves away incorrectly placed noise Gaussians that would otherwise interfere with surface reconstruction. After depth pruning, we further eroded the occupancy grid to establish a buffer distance between the Gaussians of noise and the object surface. This guarantees a minimal thickness for the surface Gaussians to optimize without noise interference.

Multi-scale noise injection. For a balanced setup to minimize computational overhead and maximize the coverage of fine geometrical features, we initiate noise Gaussians at multiple-voxel grid resolution. The initialization is repeated in a coarse-to-fine manner, where we only initialize new noise Gaussians in occupied voxels that do not already contain noise Gaussians from previous resolution levels. This allows us to fit complex geometry and finer features while maintaining low noise count.

Fine tuning. As a final refinement step, we freeze the surface Gaussians and conduct a training pass where only the opacity values of noise Gaussians are made trainable. During this phase and for the remainder of training, we randomly set the color of each noise Gaussian from Red Green Blue Cyan Magenta Yellow (RGBCMY) at each iteration. This prevents the noise opacities from overfitting to the surface’s color, ensuring they are optimized based on occlusion alone. RGBCMY is chosen because these six primary and secondary colors offer maximum contrast against most natural surface colors in RGB and HSV space. The opacity of incorrectly placed noise Gaussians (e.g., too close to the surface) decreases until they are removed through pruning. The fine tuning is a final step to guarantee no noise Gaussians interact negatively with the surface Gaussians.

Guided Surface training. Following the fine-tuning phase, the interior noise structure is considered final. We freeze all parameters of the noise Gaussians for the remainder of training. The surface Gaussians are then unfrozen, and we reset the learning rate for their means. This reset allows the

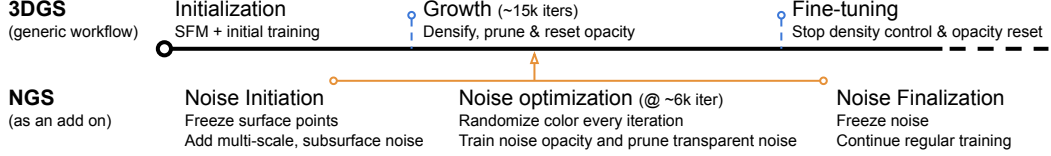


Figure 3: 3DGS training schedule with NGS. NGS is an add-on to the standard 3DGS pipeline.

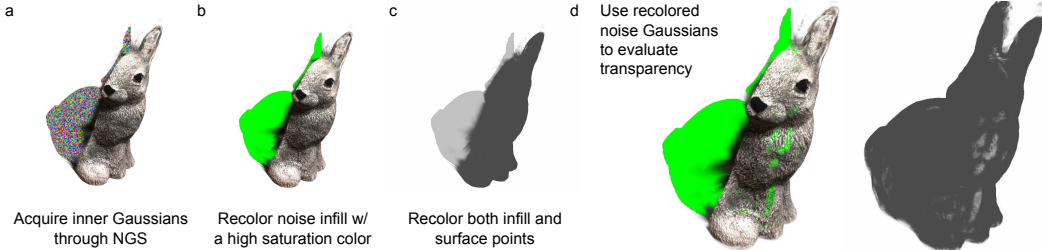


Figure 4: Noise Gaussian primitives from NGS as an infill to evaluate surface transmittance. (a) Generated and extracted noise Gaussians from NVS training. (b) Recolored noise Gaussians for transparency visualization. (c) Recolored surface and noise Gaussians for higher visual contrast and quantitative analysis. (d) Noise Gaussians inserted into models trained with other methods to characterize false transparency.

surface parameters to adapt effectively to the new optimization landscape defined by the internal noise barrier. Training then proceeds as normal, with the continued randomization of the noise Gaussians' colors preventing the surface from learning to complement a static internal pattern.

3.4 Transparency benchmark

Standard quality metrics (e.g., Peak Signal-to-Noise Ratio (PSNR), Structural Similarity Index (SSIM), and Learned Perceptual Image Patch Similarity (LPIPS)) do not quantify view inconsistency, because they are designed to work on pairs of static images. In scenarios where reconstructions exhibit false transparency, the metrics can still report high scores. Using noise Gaussian primitives created by NGS, we can create a dense point cloud placed inside the object volume that breaks the line of sight and obscures the background Gaussians during evaluation. It creates a false transparency diagnostic tool to visualize and measure the false transparency.

Visualization. For transparency visualization, we simply insert the pre-trained noise into a trained 3DGS asset and render them together using the rasterizer (Fig. 4). We can then visualize and measure the surface transparency in static renderings without interactively manipulating the 3D model to spot view inconsistency. The infill can be used to reveal transparency in the original model, or we could recolor the surface into a complementary color for better visual contrast (Fig. 4).

Quantification. To quantify the transparency, we set the infill and surface Gaussians into two solid colors (e.g., green and red). We then render the image using the standard rasterizer, and use the infill color channel as a surface transmittance map T_i for viewpoint i . The mean pixel values of the infill color channel are computed for all foreground pixels. If a segmentation mask M_i is available, we apply the mask to further refine the target area. We could also use the rendering α or recolored surface Gaussian as M_i when the segmentation mask is not available (e.g., in novel views). We define results normalized in log scale as Surface Opacity Score (SOS):

$$SOS_i = \frac{\log(\sum T_i / \sum M_i + \epsilon)}{\log(\epsilon)}, \quad (5)$$

where ϵ is set to 1E-10 to ensure numerical stability. We expect $SOS_i = 1$ for fully opaque surfaces, and $SOS_i \approx 0$ for fully transparent surfaces.

4 Experiments & results

4.1 Experimental settings

Dataset. We used public available object-centric datasets, DTU [37] and OmniObject3D [38], to evaluate NGS. To support research on high-resolution macro 3D scanning, we also captured a novel high-resolution dataset, herein referred to as the *Stone Dataset*. This dataset comprises over 100 distinct stone samples, selected for their complex geometry and surface textures, to test the robustness and detail-capturing capabilities of our approach. For the *Stone Dataset*, we acquired 240 images per sample. Each stone was positioned on a rotating turntable within a softbox. Images were captured from 6 latitudinal and 40 longitudinal angles, covering the entire upper hemisphere of the samples. Images have 3000×4000 pixels, and 16-bit raw Bayer data was preserved to retain maximum image information. Camera pose estimation for this custom dataset was performed using COLMAP [39]. For all datasets employed in our study (DTU, OmniObject3D, and the *Stone Dataset*), we also produced a high-quality foreground segmentation for each image using MVAnet [40]. Example data is shown in Fig. S1,S2&S3. All data created for this study will be made available to the community. This release includes the *Stone Dataset*, foreground segmentation masks, the generated noise infills, and a supplementary dataset featuring a mixture of everyday objects (Fig. S4).

Training. We conducted all experiments on NVIDIA L40S GPUs using the GSplat framework [41]. Unless explicitly stated, our base implementation of NGS used the default variant of GSplat. Trainings typically required no more than 8GB of VRAM. Average training time for base methods (without noise) was 16 min for DTU [37], 11 min for OmniObject3D [38], and 18 min for the new Stone dataset (15k adaptive density control + 15k refinement). Adding noise Gaussians increased memory consumption by about 50% due to the additional primitives required to fill the object interior, and increased training time by 1 min. If the memory consumption becomes a limiting factor, reducing the number of finer noise Gaussians can substantially reduce the memory consumption.

Baselines. We conducted our transparency evaluation protocol (Sect. 3.4) on several 3DGS variants, Gaussian Opacity Fields (GOF) [42], and StopThePop [6], across all three datasets (DTU, OmniObject3D, and our *Stone dataset*)

Benchmarking. A standard 7:1 train-test split was used for all datasets, with the test set forming the basis for all quantitative metrics. We first assessed quality of our result and baselines using PSNR, SSIM, and LPIPS, together with the *SOS* metric proposed in this work. To analyze the perceptual impact of any surface transparency, the standard NVS metrics were re-evaluated with pre-trained, recolored noise infill included in the rendered scene. Comparing these infill-conditioned metrics (denoted with an asterisk in Table. 1, e.g., PSNR*) against the baseline NVS scores highlights the extent to which the infill visually "leaks" through the object's surface.

4.2 Implementation details

NGS settings. The \mathcal{L}_a loss was added to the photometric loss from \mathcal{L}_{photo} to enforce α -consistency. Noise Gaussians were introduced at iteration 6,000 during adaptive density control, allowing sufficient time for the initial surface reconstruction to establish before applying our transparency guidance strategy (Fig. 3). We refined the noise Gaussians for 1,000 iterations. The surface Gaussians were frozen during noise refinement. After the noise refinement, the noise Gaussians' means, opacity, scale and rotations were frozen. Until the end of training, each noise Gaussian's color was randomized from RGBCMY at each iteration, preventing the surface Gaussians from fitting a fixed noise pattern. We reset the learning rate of Gaussian means to compensate for the sudden change to the blending. The rest of training follows the default GSplat parameters.

4.3 Object-centric 3DGS Reconstruction Evaluation

Novel view synthesis metrics and limitations. NVS metrics (PSNR, SSIM, LPIPS) effectively measure the overall visual fidelity of reconstructions but fail to specifically identify or quantify false transparency artifacts. These artifacts stem from their foreground-background ambiguity, where background elements visible through transparent surfaces contribute to the render score. This is particularly problematic for object-centric reconstruction where internal Gaussians can be optimized to match the appearance of surface Gaussians. To address this limitation, we employ our transparency evaluation protocol described in Section 3.4.

Table 1: Average NVS and *SOS* results on DTU (Table. S2), OmniObject3D (Table. S3) and our novel dataset (Table. S1). Metrics denoted by * were acquired when using a green infill, as shown in Fig. 5 and $+\alpha$ denotes use of \mathcal{L}_a .

	Method	PSNR \uparrow	PSNR* \uparrow	SSIM \uparrow	SSIM* \uparrow	LPIPS \downarrow	LPIPS* \downarrow	<i>SOS</i> \uparrow
DTU	3DGS	25.575	22.967	0.891	0.874	0.180	0.250	0.147
	GOF	25.648	21.109	0.880	0.816	0.209	0.273	0.179
	StopThePop	22.817	18.885	0.852	0.780	0.213	0.315	0.135
	GSplat $+\alpha$	25.435	25.263	0.884	0.883	0.183	0.186	0.598
	NGS	25.428	25.427	0.881	0.881	0.192	0.192	0.749
Stone	3DGS	34.610	27.551	0.949	0.909	0.055	0.222	0.140
	GOF	31.469	21.998	0.893	0.780	0.186	0.324	0.126
	StopThePop	32.457	23.047	0.945	0.853	0.078	0.223	0.168
	GSplat $+\alpha$	33.832	33.823	0.948	0.948	0.062	0.062	0.891
	NGS	34.148	34.148	0.951	0.951	0.053	0.053	0.922
OmniObject	3DGS	29.300	27.456	0.940	0.929	0.069	0.116	0.215
	GOF	32.259	24.931	0.970	0.898	0.062	0.122	0.208
	StopThePop	32.274	25.095	0.970	0.900	0.050	0.113	0.265
	GSplat $+\alpha$	33.575	33.350	0.973	0.972	0.060	0.064	0.642
	NGS	33.619	33.578	0.972	0.972	0.060	0.060	0.736

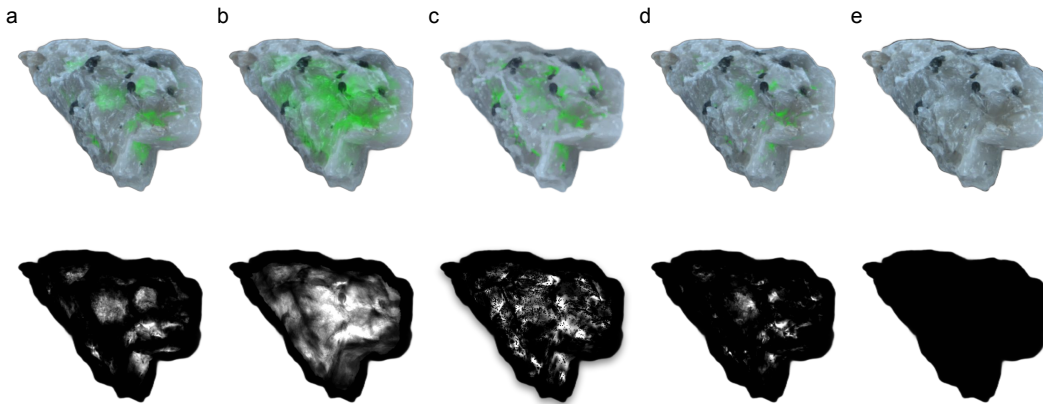


Figure 5: Renders with green infill revealing transparency (top) and corresponding transmittance maps (bottom) for (a) 3DGS, (b) GOF, (c) StopthePop, (d) Gsplat $+\alpha$ and (e) NGS.

Quantitative results. Our quantitative evaluation (Table 1) demonstrates that NGS consistently improves surface opacity across all tested methods while maintaining or slightly improving standard rendering metrics. When comparing transparency scores between baseline methods and their noise-enhanced counterparts, we observe an average reduction in surface transmittance by a factor of two, confirming the effectiveness of our approach in addressing false transparency. Notably, the introduction of noise Gaussians does not adversely affect rendering quality as measured by standard metrics, with several cases showing modest improvements in PSNR and SSIM. This suggests that by resolving the foreground-background optimization ambiguity, NGS not only reduces transparency but also helps the optimization process converge to more accurate reconstructions.

Quality comparison on challenging cases. Our evaluation demonstrates varying degrees of effectiveness across different datasets. On our *Stone* dataset, NGS almost completely eliminates false transparency artifacts (Fig. 5), resulting in fully opaque surface reconstructions. This superior performance can be attributed to the controlled capture environment with consistent, diffuse light from a softbox, which reduces view-dependent effects and provides uniform illumination across all

viewpoints. In contrast, while still showing significant improvement, NGS achieves more modest transparency reduction on the DTU and OmniObject3D datasets (Fig. S5, S6, S7 & S8). These datasets feature more variable lighting conditions with stronger directional components, creating view-dependent effects that can be misinterpreted as transparency during optimization. The inconsistent shadows and highlights across different viewpoints make it more challenging to establish a clear distinction between surface appearance variation and actual transparency. These results highlight the important relationship between lighting consistency and false transparency in 3DGS, suggesting that controlled capture conditions can substantially enhance the effectiveness of transparency reduction.

4.4 Ablation Study

To thoroughly evaluate the impact of each component in our NGS method, we conducted a series of ablation experiments using our stone dataset to isolate the effects of individual design choices on both rendering quality and transparency reduction. One at a time, we removed the following components from the proposed NGS pipeline: binary erosion, pruning, \mathcal{L}_f (from Eq. 4) and learning rate reset at noise initialization. We also substitute \mathcal{L}_f for random background. Our results (Table 2) demonstrate that the default NGS configuration achieves an optimal balance between rendering quality and transparency reduction. Among the tested variations, two components proved particularly crucial for the method’s effectiveness, learning rate reset and \mathcal{L}_f .

Learning rate reset. Resetting the learning rate decay for Gaussian means after noise introduction substantially improved the system’s ability to adapt to the new optimization landscape. Without this reset, we observed that surface Gaussians struggled to properly adjust their parameters in response to the presence of internal noise Gaussians, resulting in degraded reconstruction quality and higher transparency scores. \mathcal{L}_f outperformed alternative background regularization techniques. While random background approaches provided some mitigation of transparency issues, our foreground loss directly incentivizes surface opacity, resulting in a greater reduction in transparency scores.

Noise voxel grid erosion. We also note that although not eroding the voxel grid for noise Gaussians achieves better transparency scores, it hinders the visual quality of the renders. These ablation studies confirm that NGS’s effectiveness stems from the synergistic combination of appropriate noise guidance and targeted optimization adjustments, with the learning rate reset and foreground loss serving as the most significant contributors to its performance.

5 Discussion

Findings. Our results demonstrate that Noise Guided Splatting effectively addresses the false transparency problem in object-centric 3D Gaussian Splatting while maintaining or improving novel view synthesis quality. By injecting noise Gaussians within object volumes, we successfully force the optimization process to prioritize surface opacity, resulting in more accurate and view-consistent reconstructions. The results aligns with our theoretical understanding of the transparency problem as an optimization ambiguity between foreground and background elements.

Standard photometric losses alone cannot distinguish between a properly opaque surface and a partially transparent surface with a solid surface sitting behind. By breaking the line of sight between front and back surfaces with noise infill, we eliminate this ambiguity and guide the optimization toward solutions with appropriate surface opacity. The reduction in *SOS* across different methods and datasets confirms the generalizability of our approach. Importantly, this improvement does not come at the cost of rendering quality and even improves PSNR and SSIM in some cases. It demonstrates that resolving false transparency is not merely a visual enhancement but a fundamental improvement to the reconstruction process.

Limitations. Despite its effectiveness, NGS has several limitations worth acknowledging. First, our method benefits from high-quality segmentation masks to guide the object-centric reconstruction. Inaccurate segmentation can lead to incorrect noise Gaussian placement, potentially compromising reconstruction quality. This limitation is particularly relevant for objects with fine details or complex boundaries. Second, NGS assumes the material is fully opaque. For inherently transparent or translucent objects (e.g., glass, certain plastics), our approach may incorrectly enforce opacity where transparency is actually desired. Third, our approach requires a reasonable Gaussian point cloud to define a convex hull encompassing the entirety of the object. Fourth, while we have shown NGS’s

Table 2: Mean NVS and *SOS* scores over the *Stone Dataset*. Metrics denoted by * were acquired when using an infill. The current NGS setting provides a good balance between *SOS* and NVS metrics. Renderings of a selected stone is shown in Fig. S9

Method	PSNR \uparrow	PSNR* \uparrow	SSIM \uparrow	SSIM* \uparrow	LPIPS \downarrow	LPIPS* \downarrow	<i>SOS</i> \uparrow
Ours	32.201	32.201	0.934	0.934	0.145	0.145	0.969
w/o Erosion	30.785	30.785	0.914	0.914	0.225	0.225	1.000
w/o Pruning	31.496	31.489	0.927	0.927	0.151	0.151	0.952
w/o \mathcal{L}_f	31.252	30.930	0.928	0.927	0.126	0.135	0.379
w/o LR reset	26.136	26.133	0.830	0.830	0.416	0.416	0.545
Random Bg	30.205	30.149	0.923	0.923	0.136	0.139	0.467
w/o Color reset	31.442	31.436	0.926	0.926	0.154	0.154	0.962

effectiveness for object-centric reconstruction, its application to large-scale scene reconstruction requires further investigation. The current noise initialization and pruning strategies will require adaptation for scenes with multiple objects and complex spatial relationships. Finally, this method is less effective for thin structures where injecting noise is difficult.

Computational Considerations. NGS introduces some computational overhead relative to standard 3DGs, primarily in the form of increased memory requirements and rendering time during training. The number of additional noise Gaussians depends on object geometry complexity, typically increasing the total Gaussian count by 30-50%. This translates to proportional increases in memory usage and rendering time. However, several optimizations could mitigate these costs. Our multi-resolution initialization approach already reduces the number of required noise Gaussians compared to uniform voxel filling. Further improvements include reducing the parameters for noise Gaussians down to spheres with variable opacity and color, removing spherical harmonics, quaternions and scales.

Broader Applications. The improved surface consistency provided by NGS has significant implications for several downstream applications. In AR/VR asset creation, where accurate object representation is critical for immersive experiences, our method produces more reliable reconstructions with well-defined boundaries. The reduced transparency particularly benefits applications requiring watertight meshes, such as physics simulations or 3D printing. By providing clearer surface definitions, NGS reduces the need for manual cleanup of extracted meshes, streamlining the transition from digital reconstruction to physical reproduction. It is also worth noting that while NGS effectively addresses the false transparency problem, future research may develop alternative approaches to resolve this issue. Nevertheless, the infill assets generated by NGS can still serve a valuable purpose. They provide a robust basis for the *SOS* benchmark, thereby facilitating the evaluation and comparison of subsequent methods aimed at mitigating false transparency, regardless of their underlying technique.

Future Directions. Extending our method to more complex scenes containing multiple objects using segmentation methods like Segment Any 3D Gaussians [43] to isolate each object and apply our NGS pipeline individually. Another promising research direction to emerge from this work is to use the noise infill as learnable interior Gaussians and predict the internal structures of the model. For example, FruitNinja [44] used infill particles together with a diffusion model to generate the internal structures of 3D models. The noise infill provide a more robust way for initializing these method.

References

- [1] Bernhard Kerbl, Georgios Kopanas, Thomas Leimkühler, and George Drettakis. 3d gaussian splatting for real-time radiance field rendering. *ACM Transactions on Graphics*, 42(4), July 2023.
- [2] Qiqi Hou, Randall Rauwendaal, Zifeng Li, Hoang Le, Farzad Farhadzadeh, Fatih Porikli, Alexei Bourd, and Amir Said. Sort-free gaussian splatting via weighted sum rendering, 2025.
- [3] Shakiba Kheradmand, Delio Vicini, George Kopanas, Dmitry Lagun, Kwang Moo Yi, Mark Matthews, and Andrea Tagliasacchi. Stochasticsplats: Stochastic rasterization for sorting-free 3d gaussian splatting, 2025.
- [4] Michael Steiner, Thomas Köhler, Lukas Radl, Felix Windisch, Dieter Schmalstieg, and Markus Steinberger. Aaa-gaussians: Anti-aliased and artifact-free 3d gaussian rendering, 2025.
- [5] Florian Hahlbohm, Fabian Friederichs, Tim Weyrich, Linus Franke, Moritz Kappel, Susana Castillo, Marc Stamminger, Martin Eisemann, and Marcus Magnor. Efficient perspective-correct 3d gaussian splatting using hybrid transparency. *Computer Graphics Forum*, 44(2), 2025.
- [6] Lukas Radl, Michael Steiner, Mathias Parger, Alexander Weinrauch, Bernhard Kerbl, and Markus Steinberger. StopThePop: Sorted Gaussian Splatting for View-Consistent Real-time Rendering. *ACM Transactions on Graphics*, 43(4), 2024.
- [7] Ben Mildenhall, Pratul P. Srinivasan, Matthew Tancik, Jonathan T. Barron, Ravi Ramamoorthi, and Ren Ng. Nerf: Representing scenes as neural radiance fields for view synthesis, 2020.
- [8] Jiakai Sun, Zhanjie Zhang, Jiafu Chen, Guangyuan Li, Boyan Ji, Lei Zhao, Wei Xing, and Huaizhong Lin. Vgos: Voxel grid optimization for view synthesis from sparse inputs, 2023.
- [9] Thomas Müller, Alex Evans, Christoph Schied, and Alexander Keller. Instant neural graphics primitives with a multiresolution hash encoding. *ACM Trans. Graph.*, 41(4):102:1–102:15, July 2022.
- [10] Saswat Subhajyoti Mallick, Rahul Goel, Bernhard Kerbl, Francisco Vicente Carrasco, Markus Steinberger, and Fernando De La Torre. Taming 3dgs: High-quality radiance fields with limited resources, 2024.
- [11] Tao Lu, Ankit Dhiman, Srinath R, Emre Arslan, Angela Xing, Yuanbo Xiangli, Venkatesh Babu Radhakrishnan, and Srinath Sridhar. Turbo-gs: Accelerating 3d gaussian fitting for high-quality radiance fields, 2024.
- [12] Samuel Rota Bulò, Lorenzo Porzi, and Peter Kortschieder. Revising densification in gaussian splatting, 2024.
- [13] Zehao Yu, Anpei Chen, Binbin Huang, Torsten Sattler, and Andreas Geiger. Mip-splatting: Alias-free 3d gaussian splatting. *Conference on Computer Vision and Pattern Recognition (CVPR)*, 2024.
- [14] Shakiba Kheradmand, Daniel Rebain, Gopal Sharma, Weiwei Sun, Jeff Tseng, Hossam Isack, Abhishek Kar, Andrea Tagliasacchi, and Kwang Moo Yi. 3d gaussian splatting as markov chain monte carlo, 2025.
- [15] Luchao Wang, Qian Ren, Kaimin Liao, Hua Wang, Zhi Chen, and Yaohua Tang. Stablegs: A floater-free framework for 3d gaussian splatting, 2025.
- [16] Leo Segre and Shai Avidan. Optimize the unseen – fast nerf cleanup with free space prior, 2024.
- [17] Baowen Zhang, Chuan Fang, Rakesh Shrestha, Yixun Liang, Xiaoxiao Long, and Ping Tan. Rade-gs: Rasterizing depth in gaussian splatting, 2024.
- [18] Frederik Warburg*, Ethan Weber*, Matthew Tancik, Aleksander Hołyński, and Angjoo Kanazawa. Nerfbusters: Removing ghostly artifacts from casually captured nerfs. In *International Conference on Computer Vision (ICCV)*, 2023.

- [19] Yunzhou Song, Heguang Lin, Jiahui Lei, Lingjie Liu, and Kostas Daniilidis. Hdgs: Textured 2d gaussian splatting for enhanced scene rendering, 2024.
- [20] Junha Hyung, Susung Hong, Sungwon Hwang, Jaeseong Lee, Jaegul Choo, and Jin-Hwa Kim. Effective rank analysis and regularization for enhanced 3d gaussian splatting, 2024.
- [21] Jay Zhangjie Wu, Yuxuan Zhang, Haithem Turki, Xuanchi Ren, Jun Gao, Mike Zheng Shou, Sanja Fidler, Zan Gojcic, and Huan Ling. Difix3d+: Improving 3d reconstructions with single-step diffusion models. *arXiv preprint arXiv: 2503.01774*, 2025.
- [22] Mingwei Li, Pu Pang, Hehe Fan, Hua Huang, and Yi Yang. Tsgs: Improving gaussian splatting for transparent surface reconstruction via normal and de-lighting priors, 2025.
- [23] Jeongyun Kim, Jeongho Noh, Dong-Guw Lee, and Ayoung Kim. Transplat: Surface embedding-guided 3d gaussian splatting for transparent object manipulation, 2025.
- [24] Letian Huang, Dongwei Ye, Jialin Dan, Chengzhi Tao, Huiwen Liu, Kun Zhou, Bo Ren, Yuanqi Li, Yanwen Guo, and Jie Guo. Transparentgs: Fast inverse rendering of transparent objects with gaussians. *ACM Transactions on Graphics*, 2025.
- [25] Marcel Rogge and Didier Stricker. Object-centric 2d gaussian splatting: Background removal and occlusion-aware pruning for compact object models. In *Proceedings of the 14th International Conference on Pattern Recognition Applications and Methods*, page 519–530. SCITEPRESS - Science and Technology Publications, 2025.
- [26] Jiazhong Cen, Jiemin Fang, Chen Yang, Lingxi Xie, Xiaopeng Zhang, Wei Shen, and Qi Tian. Segment any 3d gaussians, 2025.
- [27] Umangi Jain, Ashkan Mirzaei, and Igor Gilitschenski. Gaussiancut: Interactive segmentation via graph cut for 3d gaussian splatting. In *The Thirty-eighth Annual Conference on Neural Information Processing Systems*, 2024.
- [28] Justin Yu, Kush Hari, Kishore Srinivas, Karim El-Refai, Adam Rashid, Chung Min Kim, Justin Kerr, Richard Cheng, Muhammad Zubair Irshad, Ashwin Balakrishna, Thomas Kollar, and Ken Goldberg. Language-embedded gaussian splats (legs): Incrementally building room-scale representations with a mobile robot, 2024.
- [29] Minghan Qin, Wanhu Li, Jiawei Zhou, Haoqian Wang, and Hanspeter Pfister. Langsplat: 3d language gaussian splatting, 2024.
- [30] Ri-Zhao Qiu, Ge Yang, Weijia Zeng, and Xiaolong Wang. Feature splatting: Language-driven physics-based scene synthesis and editing, 2024.
- [31] Shijie Zhou, Haoran Chang, Sicheng Jiang, Zhiwen Fan, Zehao Zhu, Dejia Xu, Pradyumna Chari, Suya You, Zhangyang Wang, and Achuta Kadambi. Feature 3dgs: Supercharging 3d gaussian splatting to enable distilled feature fields, 2024.
- [32] Justin Yu, Kush Hari, Karim El-Refai, Arnav Dalil, Justin Kerr, Chung-Min Kim, Richard Cheng, Muhammad Z. Irshad, and Ken Goldberg. Persistent object gaussian splat (pogs) for tracking human and robot manipulation of irregularly shaped objects. *ICRA*, 2025.
- [33] Siting Zhu, Guangming Wang, Xin Kong, Dezhi Kong, and Hesheng Wang. 3d gaussian splatting in robotics: A survey, 2024.
- [34] Liu Liu, Xinjie Wang, Jiaxiong Qiu, Tianwei Lin, Xiaolin Zhou, and Zhizhong Su. Gaussian object carver: Object-compositional gaussian splatting with surfaces completion, 2024.
- [35] Francesco Palandra, Andrea Sanchietti, Daniele Baieri, and Emanuele Rodolà. Gsedit: Efficient text-guided editing of 3d objects via gaussian splatting, 2024.
- [36] C. Bradford Barber, David P. Dobkin, and Hannu Huhdanpaa. The quickhull algorithm for convex hulls. *ACM Trans. Math. Softw.*, 22(4):469–483, December 1996.

- [37] Rasmus Jensen, Anders Dahl, George Vogiatzis, Engil Tola, and Henrik Aanæs. Large scale multi-view stereopsis evaluation. In *2014 IEEE Conference on Computer Vision and Pattern Recognition*, pages 406–413. IEEE, 2014.
- [38] Tong Wu, Jiarui Zhang, Xiao Fu, Yuxin Wang, Liang Pan Jiawei Ren, Wayne Wu, Lei Yang, Jiaqi Wang, Chen Qian, Dahua Lin, and Ziwei Liu. Omniobject3d: Large-vocabulary 3d object dataset for realistic perception, reconstruction and generation. In *IEEE/CVF Conference on Computer Vision and Pattern Recognition (CVPR)*, 2023.
- [39] Johannes Lutz Schönberger and Jan-Michael Frahm. Structure-from-motion revisited. In *Conference on Computer Vision and Pattern Recognition (CVPR)*, 2016.
- [40] Qian Yu, Xiaoqi Zhao, Youwei Pang, Lihe Zhang, and Huchuan Lu. Multi-view aggregation network for dichotomous image segmentation. In *Proceedings of the IEEE/CVF Conference on Computer Vision and Pattern Recognition*, pages 3921–3930, 2024.
- [41] Vickie Ye, Rui long Li, Justin Kerr, Matias Turkulainen, Brent Yi, Zhuoyang Pan, Otto Seiskari, Jianbo Ye, Jeffrey Hu, Matthew Tancik, and Angjoo Kanazawa. gsplat: An open-source library for gaussian splatting. *Journal of Machine Learning Research*, 26(34):1–17, 2025.
- [42] Zehao Yu, Torsten Sattler, and Andreas Geiger. Gaussian opacity fields: Efficient adaptive surface reconstruction in unbounded scenes. *ACM Transactions on Graphics*, 2024.
- [43] Jiazhong Cen, Jiemin Fang, Chen Yang, Lingxi Xie, Xiaopeng Zhang, Wei Shen, and Qi Tian. Segment any 3d gaussians. *arXiv preprint arXiv:2312.00860*, 2023.
- [44] Fangyu Wu and Yuhao Chen. Fruitninja: 3d object interior texture generation with gaussian splatting, 2024.

A Appendix / Acronyms

3DGS 3D Gaussian Splatting

NGS Noise Guided Splatting

PSNR Peak Signal-to-Noise Ratio

SSIM Structural Similarity Index

LPIPS Learned Perceptual Image Patch Similarity

RGBCMY Red Green Blue Cyan Magenta Yellow

NeRF Neural Radiance Fields

NVS Novel View Synthesis

SOS Surface Opacity Score

MCMC Markov Chain Monte Carlo

GOF Gaussian Opacity Fields

ADC Adaptive Density Control

IQA Image Quality Assessment

B Appendix / Evaluation Results

Table S1: Full NVS and *SOS* results on our novel dataset. Metrics denoted by * were acquired when using an infill, as shown in Fig. 5 and $+\alpha$ denotes use of \mathcal{L}_a .

Index	Method	PSNR	PSNR*	SSIM	SSIM*	LPIPS	LPIPS*	<i>SOS</i>	N° Gaussians
1	NGS	32.563	32.563	0.947	0.947	0.062	0.062	1.000	585856
	Gsplat $+\alpha$	32.260	32.260	0.943	0.943	0.069	0.069	1.000	551437
2	NGS	36.229	36.229	0.956	0.956	0.043	0.043	1.000	575300
	Gsplat $+\alpha$	35.968	35.968	0.954	0.954	0.050	0.050	1.000	479522
3	NGS	33.418	33.418	0.945	0.945	0.071	0.071	0.926	591907
	Gsplat $+\alpha$	33.168	33.168	0.942	0.942	0.081	0.081	0.835	476246
4	NGS	36.244	36.244	0.962	0.962	0.046	0.046	0.953	554600
	Gsplat $+\alpha$	35.814	35.814	0.957	0.957	0.055	0.055	0.949	453943
5	NGS	32.871	32.871	0.953	0.953	0.053	0.053	0.958	542696
	Gsplat $+\alpha$	32.703	32.703	0.951	0.951	0.061	0.061	0.927	442430
6	NGS	33.302	33.302	0.940	0.940	0.057	0.057	0.626	615372
	Gsplat $+\alpha$	32.996	32.992	0.937	0.937	0.062	0.063	0.495	484779
7	NGS	32.993	32.993	0.947	0.947	0.053	0.053	0.913	540734
	Gsplat $+\alpha$	32.785	32.785	0.944	0.944	0.061	0.061	0.912	423754
8	NGS	33.153	33.153	0.948	0.948	0.042	0.042	0.995	571105
	Gsplat $+\alpha$	32.826	32.826	0.945	0.945	0.049	0.049	0.975	428108
9	NGS	36.517	36.517	0.960	0.960	0.048	0.048	0.961	585541
	Gsplat $+\alpha$	35.973	35.972	0.956	0.956	0.058	0.058	0.950	502017
10	NGS	34.193	34.186	0.951	0.951	0.057	0.057	0.890	564590
	Gsplat $+\alpha$	33.823	33.739	0.947	0.947	0.070	0.071	0.872	435205
Mean	NGS	34.148	34.148	0.951	0.951	0.053	0.053	0.922	572770
	Gsplat $+\alpha$	33.832	33.823	0.948	0.948	0.062	0.062	0.891	467744
Std.	NGS	1.565	1.565	0.007	0.007	0.009	0.009	0.111	23220
	Gsplat $+\alpha$	1.493	1.494	0.007	0.007	0.010	0.010	0.149	39548

Scan indices correspond to the following files: (1) scan_20250416_093245, (2) scan_20250416_140345, (3) scan_20250416_143850, (4) scan_20250416_151813, (5) scan_20250416_161137, (6) scan_20250416_165925, (7) scan_20250417_101115, (8) scan_20250417_112354, (9) scan_20250417_150930, (10) scan_20250417_153612

Table S2: Full NVS and *SOS* results on DTU. Metrics denoted by * were acquired when using a green infill, as shown in Fig. 5 and $+\alpha$ denotes use of \mathcal{L}_a .

	Method	PSNR	PSNR*	SSIM	SSIM*	LPIPS	LPIPS*	<i>SOS</i>	N° Gaussians
1	NGS	24.359	24.359	0.903	0.903	0.097	0.097	0.888	1461500
	Gsplat $+\alpha$	24.372	24.365	0.905	0.905	0.092	0.093	0.773	2113100
2	NGS	22.896	22.894	0.888	0.888	0.227	0.227	0.585	404102
	Gsplat $+\alpha$	22.787	22.283	0.890	0.887	0.220	0.229	0.418	566632
3	NGS	24.450	24.450	0.880	0.880	0.234	0.234	0.475	495216
	Gsplat $+\alpha$	24.390	24.280	0.880	0.880	0.228	0.231	0.318	692157
4	NGS	27.541	27.541	0.905	0.905	0.148	0.148	0.953	782621
	Gsplat $+\alpha$	27.679	27.679	0.909	0.909	0.139	0.139	0.978	1249151
5	NGS	25.682	25.682	0.877	0.877	0.196	0.196	0.791	567251
	Gsplat $+\alpha$	25.609	25.515	0.878	0.878	0.187	0.189	0.367	859701
6	NGS	28.532	28.529	0.894	0.894	0.187	0.188	0.552	642402
	Gsplat $+\alpha$	28.525	28.036	0.897	0.894	0.177	0.185	0.443	1007084
7	NGS	24.532	24.532	0.821	0.821	0.253	0.253	0.999	633185
	Gsplat $+\alpha$	24.681	24.681	0.827	0.827	0.238	0.238	0.890	839702
Mean	NGS	25.428	25.427	0.881	0.881	0.192	0.192	0.749	712325
	Gsplat $+\alpha$	25.435	25.263	0.884	0.883	0.183	0.186	0.598	1046790
Std.	NGS	1.978	1.978	0.029	0.029	0.054	0.054	0.211	351317
	Gsplat $+\alpha$	2.017	2.024	0.027	0.027	0.053	0.054	0.273	518612

Scan indices correspond to the following files: (1) scan55, (2) scan65, (3) scan69, (4) scan106, (5) scan114, (6) scan118, (7) scan122

Table S3: Full NVS and *SOS* results on OmniObject3D. Metrics denoted by * were acquired when using a green infill, as shown in Fig. 5 and $+\alpha$ denotes use of \mathcal{L}_a .

	Method	PSNR	PSNR*	SSIM	SSIM*	LPIPS	LPIPS*	<i>SOS</i>	N° Gaussians
1	NGS	35.848	35.608	0.975	0.975	0.098	0.100	0.555	191628
	Gsplat $+\alpha$	35.825	35.157	0.976	0.975	0.095	0.105	0.402	250896
2	NGS	31.690	31.690	0.978	0.978	0.039	0.039	0.806	223903
	Gsplat $+\alpha$	31.637	31.598	0.978	0.978	0.040	0.041	0.605	279212
3	NGS	35.682	35.671	0.980	0.980	0.020	0.020	0.817	123827
	Gsplat $+\alpha$	35.673	35.663	0.981	0.981	0.020	0.020	0.837	169815
4	NGS	37.958	37.958	0.972	0.972	0.083	0.083	1.000	231004
	Gsplat $+\alpha$	37.894	37.894	0.972	0.972	0.082	0.082	1.000	300919
5	NGS	33.284	33.283	0.977	0.977	0.045	0.045	0.439	274345
	Gsplat $+\alpha$	33.212	32.431	0.978	0.976	0.044	0.055	0.324	343927
6	NGS	32.178	32.178	0.972	0.972	0.048	0.048	0.834	223486
	Gsplat $+\alpha$	32.124	32.124	0.972	0.972	0.048	0.048	0.825	272385
7	NGS	28.693	28.658	0.953	0.953	0.085	0.088	0.699	268095
	Gsplat $+\alpha$	28.663	28.583	0.954	0.954	0.089	0.096	0.504	332044
Mean	NGS	33.619	33.578	0.972	0.972	0.060	0.060	0.736	219469.714
	Gsplat $+\alpha$	33.575	33.350	0.973	0.972	0.060	0.064	0.642	278456.857
Std.	NGS	3.115	3.096	0.009	0.009	0.029	0.030	0.188	50772.745
	Gsplat $+\alpha$	3.115	3.093	0.009	0.009	0.029	0.031	0.251	58112.765

Scan indices correspond to the following files: (1) antique_004, (2) dinosaur_004, (3) dinosaur_005, (4) antique_005, (5) dinosaur_006, (6) dinosaur_007, (7) dinosaur_008

C Appendix / Supplementary Figures

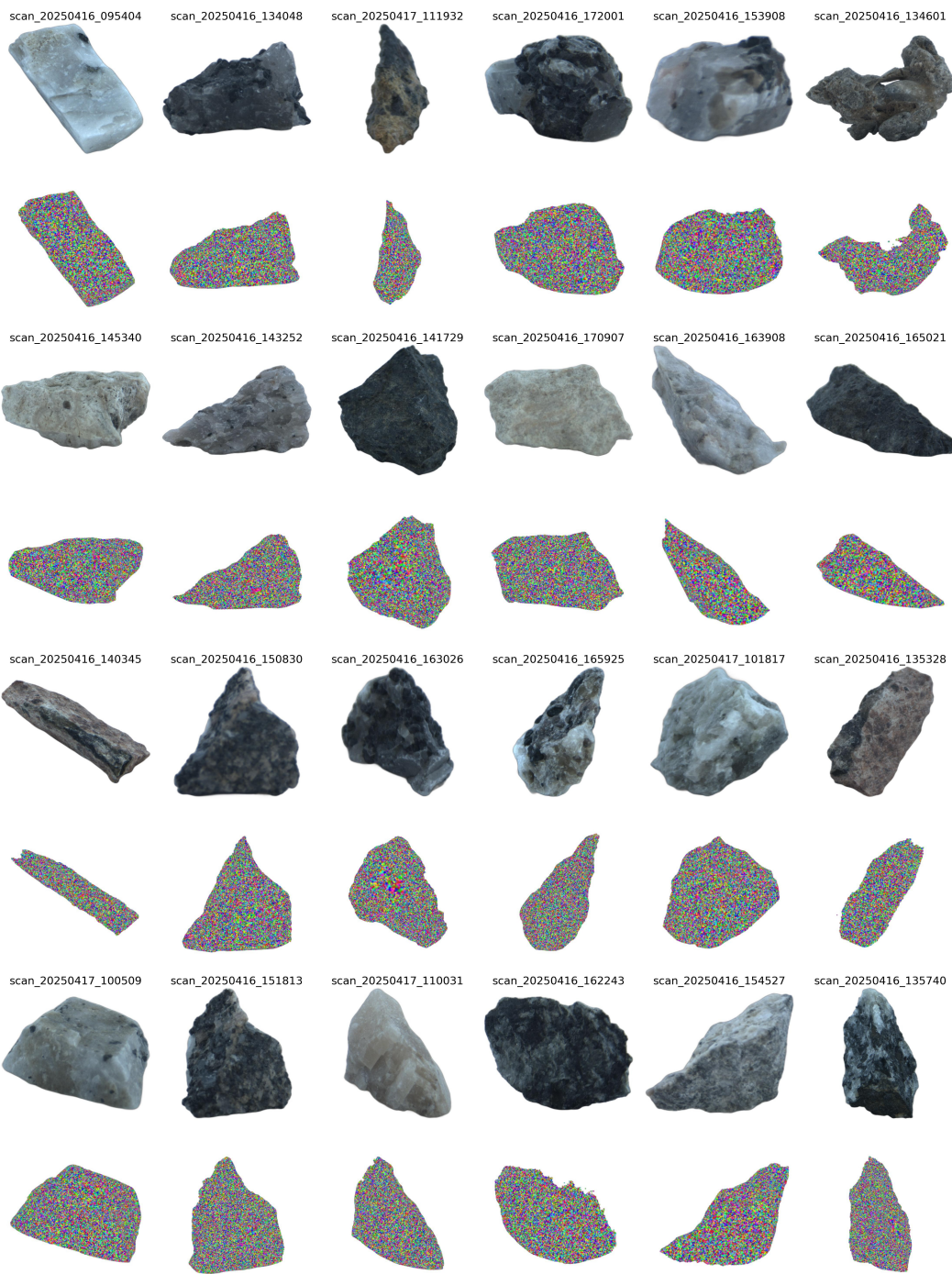


Figure S1: Stone dataset with noise augmentations



Figure S2: DTU noise augmentation

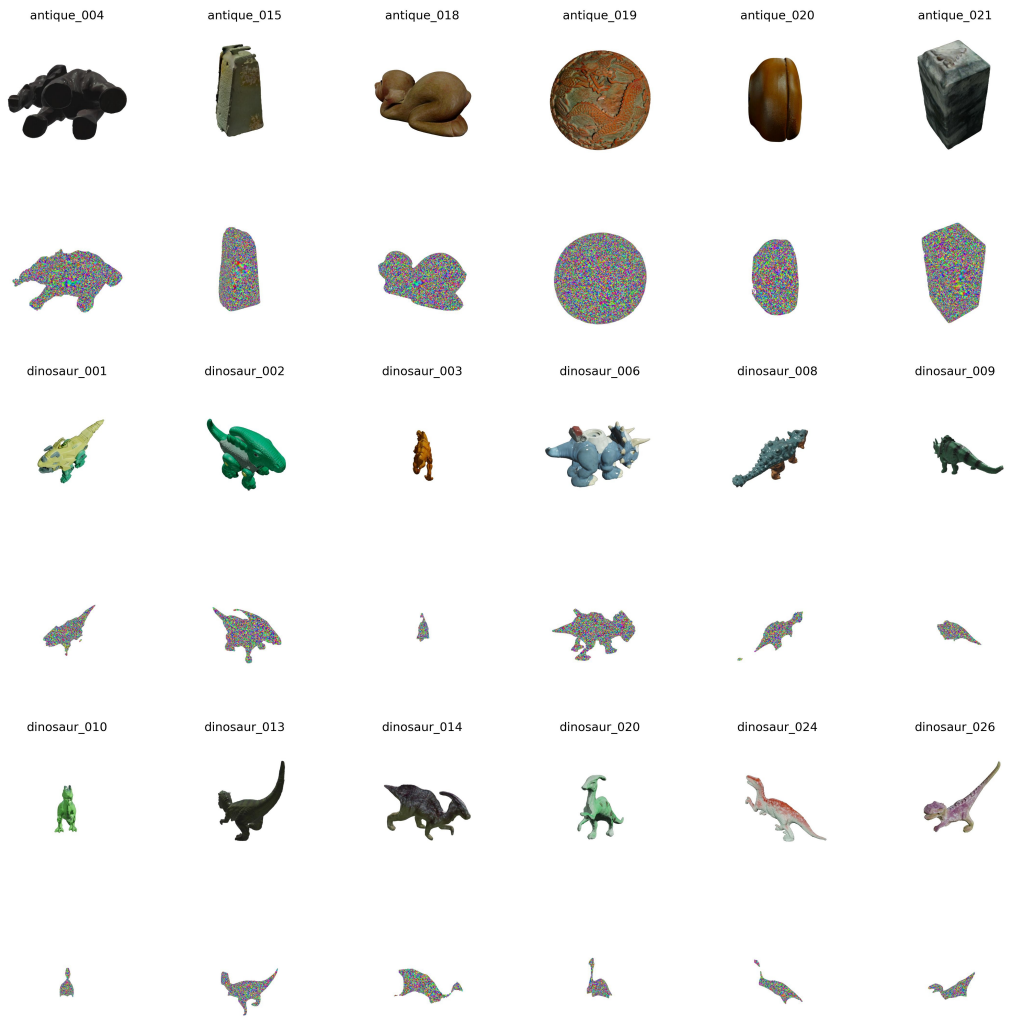
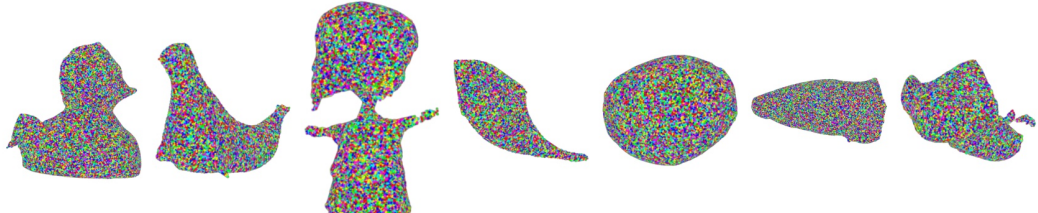
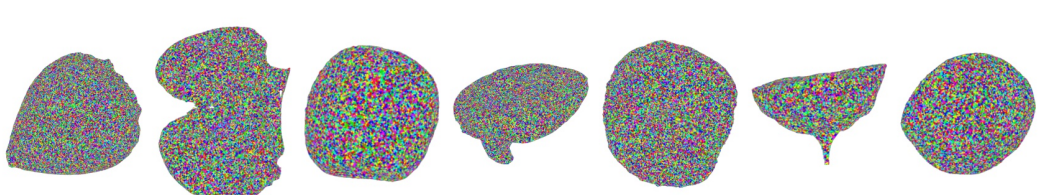


Figure S3: OmniObject3D noise augmentation

scan_20250720_145843 scan_20250720_155004 scan_20250720_144401 scan_20250720_155330 scan_20250720_145630 scan_20250720_155643 scan_20250720_153535



scan_20250713_155826 scan_20250720_143824 scan_20250720_152214 scan_20250720_154008 scan_20250715_175153 scan_20250714_174819 scan_20250720_152305



scan_20250720_155059 scan_20250720_141359 scan_20250720_143408 scan_20250720_153240 scan_20250720_150550 scan_20250720_150445 scan_20250720_142502



Figure S4: Object dataset with noise augmentation

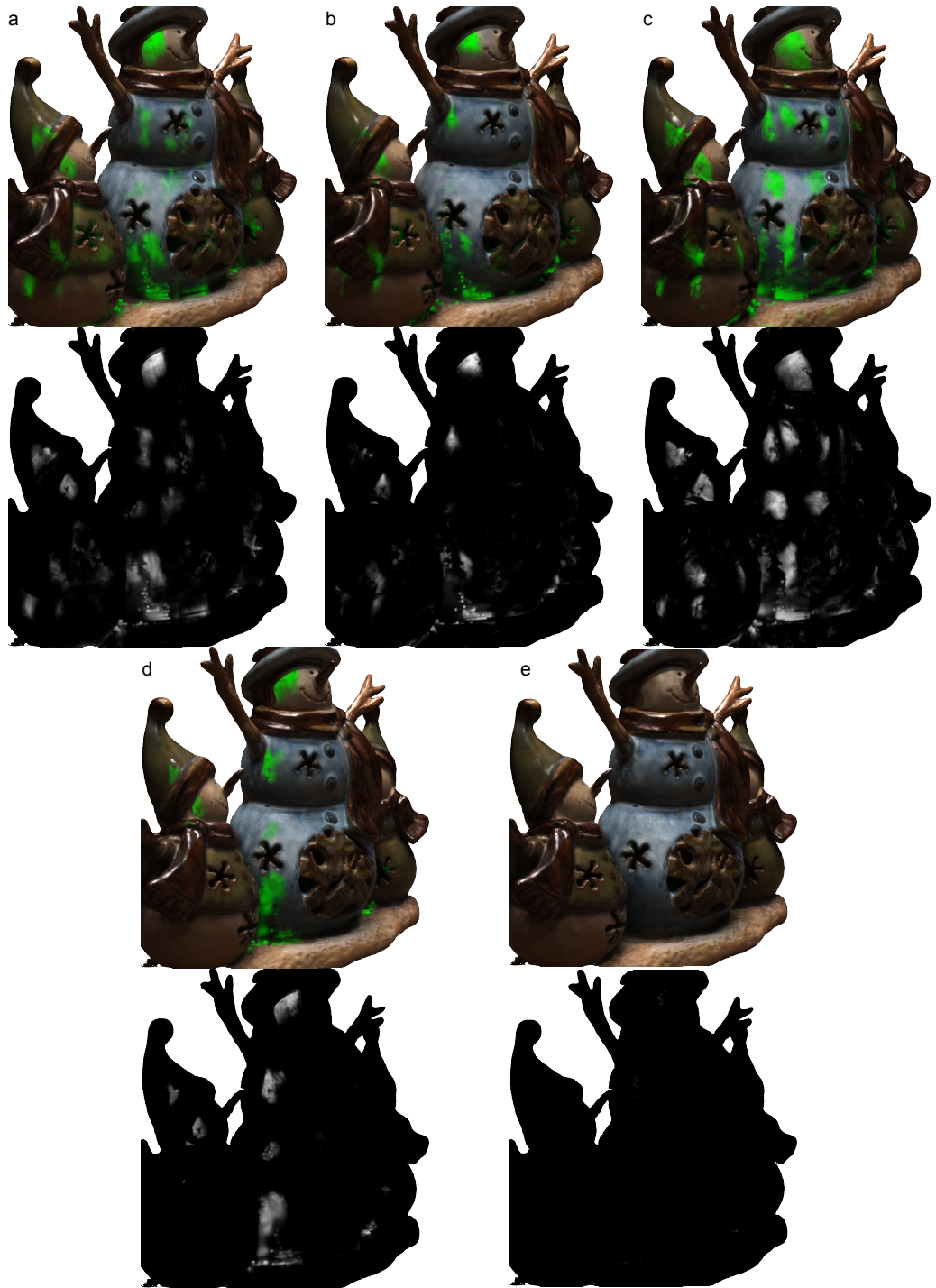


Figure S5: DTU renders with green infill revealing transparency (top) and corresponding transmittance maps (bottom) for (a) 3DGS, (b) GOF, (c) StopthePop, (d) Gsplat+ α and (e) NGS.

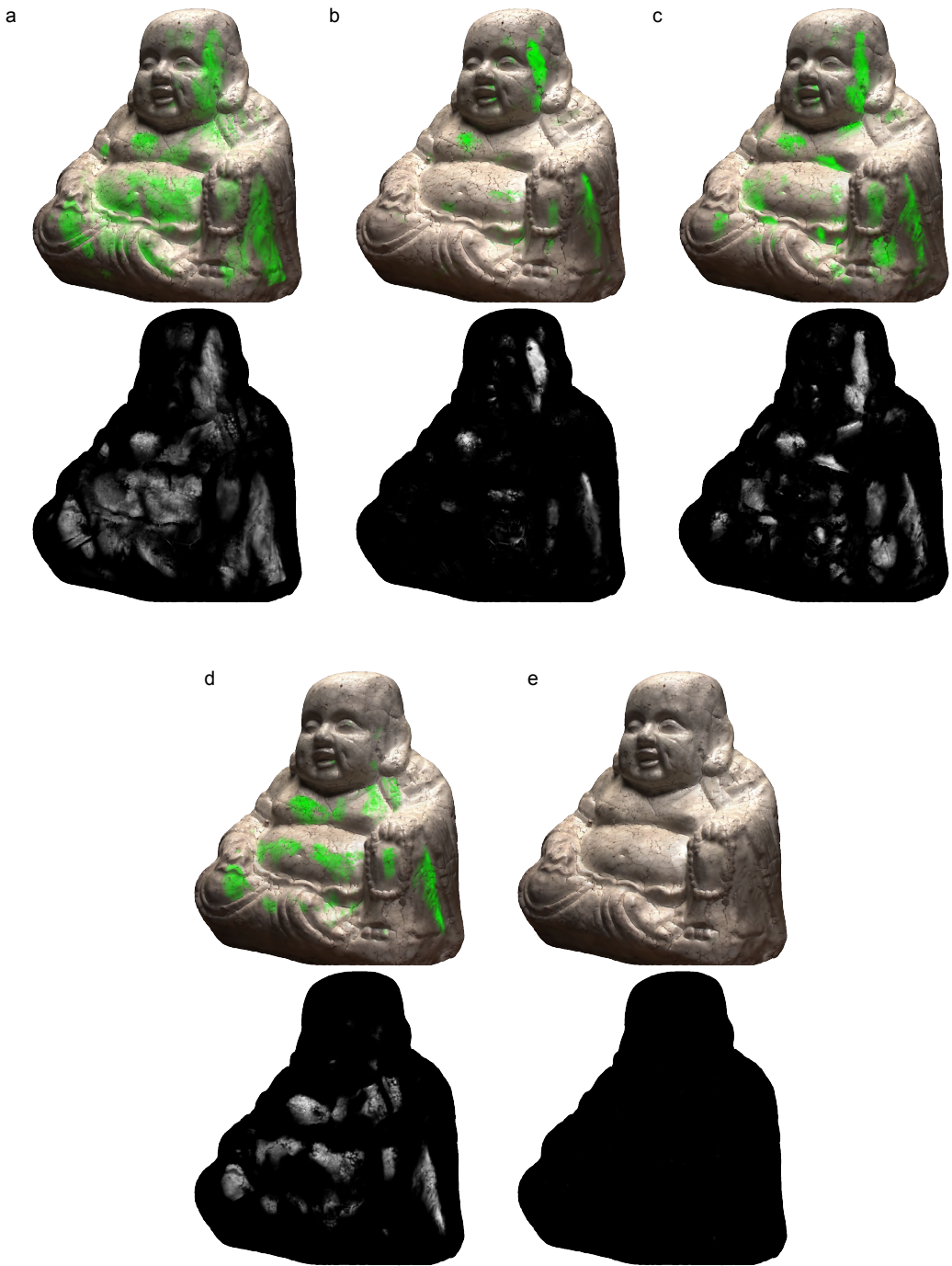


Figure S6: DTU renders with green infill revealing transparency (top) and corresponding transmittance maps (bottom) for (a) 3DGS, (b) GOF, (c) StopthePop, (d) Gsplat+ α and (e) NGS.

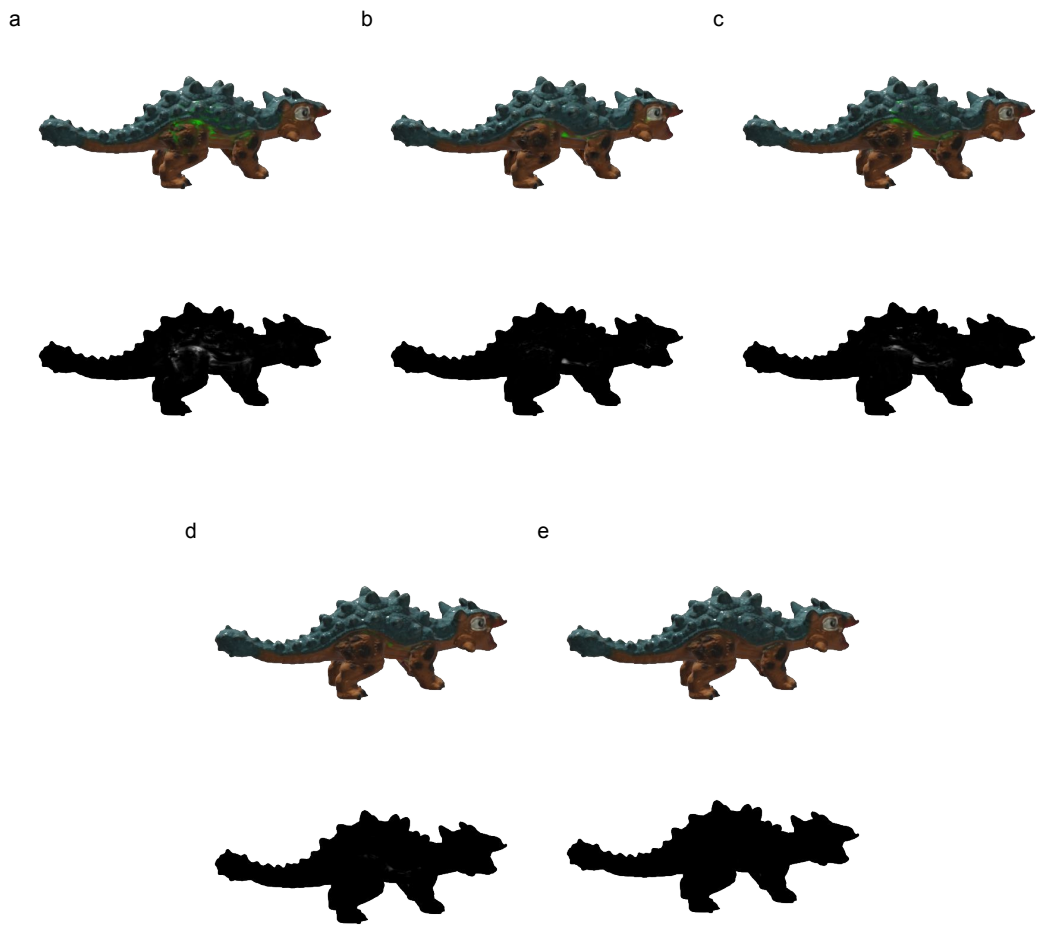


Figure S7: OmniObject3D renders with green infill revealing transparency (top) and corresponding transmittance maps (bottom) for (a) 3DGS, (b) GOF, (c) StopthePop, (d) Gsplat+ α and (e) NGS.

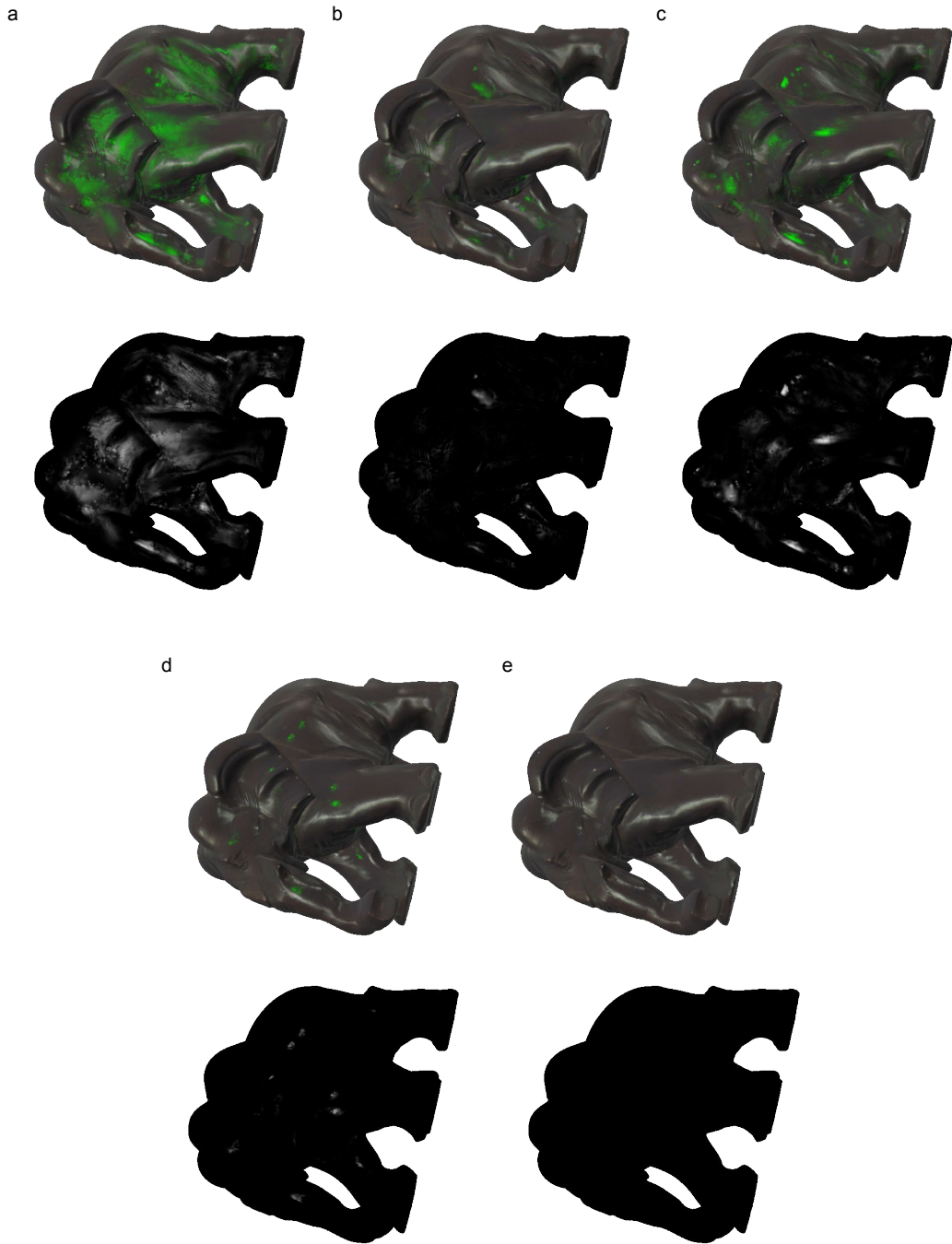


Figure S8: OmniObject3D renders with green infill revealing transparency (top) and corresponding transmittance maps (bottom) for (a) 3DGS, (b) GOF, (c) StopthePop, (d) Gsplat+ α and (e) NGS.

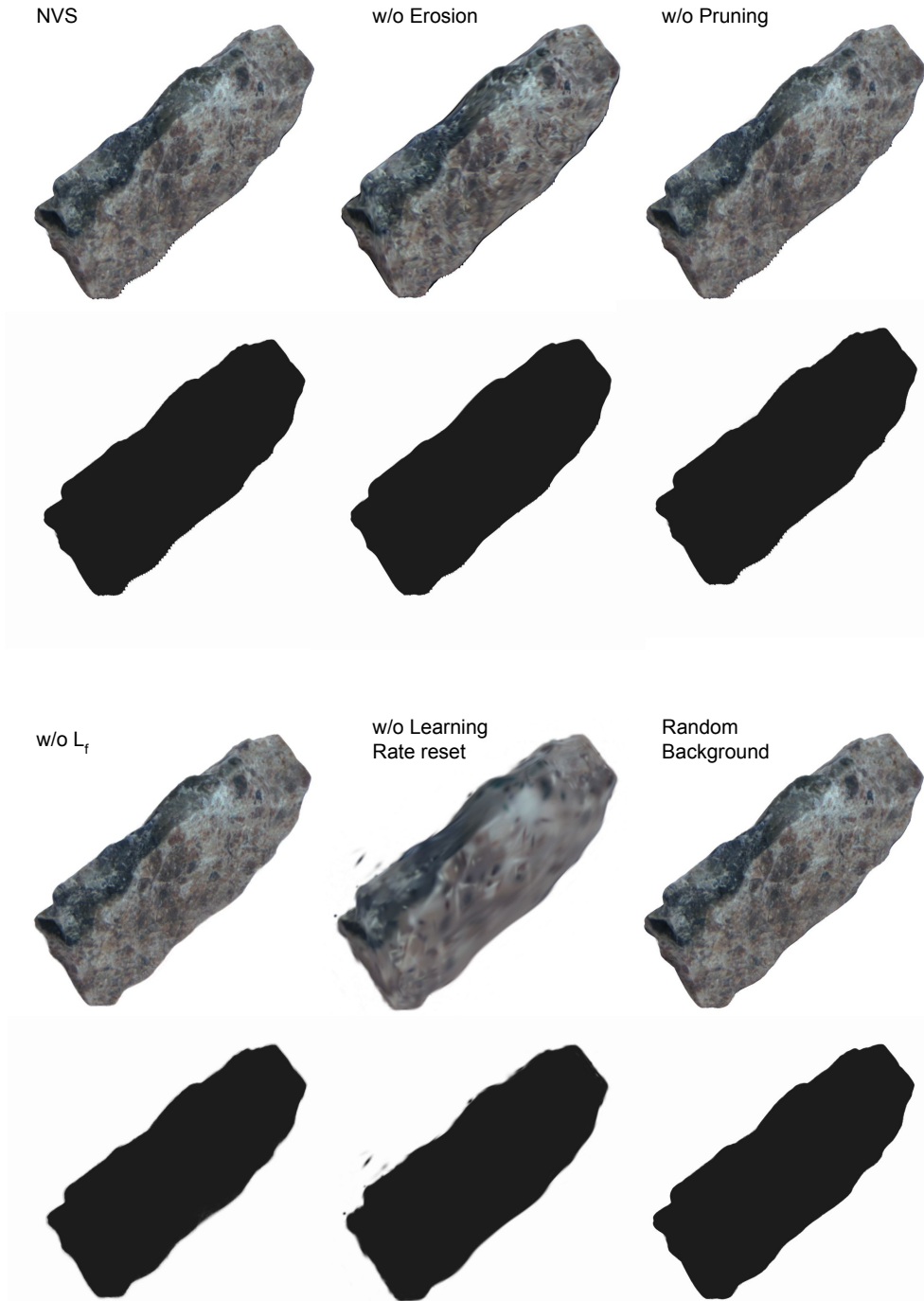


Figure S9: A sample from the *Stone Dataset* used in the ablation study. The reconstructions are filled with green noise. Reset the learning rate affects the quality of final rendering the most significantly. Stopping erosion also reduces the surface quality. Most of the result does not show visible false transparency, but the *SOS* can be quantified and compared.